

See discussions, stats, and author profiles for this publication at: <https://www.researchgate.net/publication/234020828>

Mechanical, thermal, and rheological properties of graphene-based polypropylene nanocomposites prepared by melt mixing

ARTICLE · MAY 2012

DOI: 10.1002/pc.22198

CITATIONS

41

READS

69

6 AUTHORS, INCLUDING:



Mounir El Achaby

Université Mohammed VI Polytechnique, Be...

20 PUBLICATIONS 291 CITATIONS

SEE PROFILE



Sebastien Vaudreuil

Université Euro-Méditerranéenne de Fès

22 PUBLICATIONS 414 CITATIONS

SEE PROFILE

Mechanical, Thermal, and Rheological Properties of Graphene-Based Polypropylene Nanocomposites Prepared by Melt Mixing

Mounir El Achaby,^{1,2} Fatima-Ezzahra Arrakhiz,^{1,2} Sébastien Vaudreuil,¹
Abou el Kacem Qaiss,¹ Mostapha Bousmina,³ Omar Fassi-Fehri^{3,4}

¹Moroccan Foundation for Advanced Science, Innovation and Research (MAsCIR), ENSET,
Av. Armée Royale, 10100 Rabat, Morocco

²Faculty of Sciences, Mohammed V-Agdal University, Rabat, Morocco

³Hassan II Academy of Science and Technology, Rabat, Morocco

⁴LM, Faculty of Sciences, Mohammed V-Agdal University, Rabat, Morocco

In this article, we describe the fabrication by melt mixing of graphene-polypropylene nanocomposites and present the effect of graphene addition on some selected properties of polypropylene (PP). The graphene nanosheets (GNs) used as nano-reinforcing agents were obtained through chemical reduction of graphene oxide by hydrazine hydrate. GNs were characterized and successfully dispersed into PP matrix to produce PP/GNs nanocomposites. The effects of GNs content on thermal, mechanical, and rheological properties were reported, and the obtained results were discussed in terms of morphology and state of dispersion and distribution of the GNs within the polymer matrix. Characterization by scanning electron microscopy and X-ray diffraction of the nanocomposites has shown a relatively good dispersion of GNs in the polymer matrix, with the presence of only few aggregates. Increasing GNs content resulted in a significant increase in both mechanical and thermal properties with only few percent of GNs loading. Rheological behavior of the PP/GNs nanocomposites showed a Maxwellian-like behavior for low GNs concentrations and a viscoelastic solid-like behavior for GNs content exceeding the concentration of the percolation threshold. POLYM. COMPOS., 33:733–744, 2012. © 2012 Society of Plastics Engineers

INTRODUCTION

Because of their unique mechanical, electrical, optical, and thermal properties, the various allotropes of carbon

such as diamond, graphite, graphene, and fullerene with various geometrical shapes (spherical, ellipsoidal, layered, single sheet, tubes, and buds) have attracted enormous interest from both scientific and engineering standpoints. They have extraordinary potential applications in electronics, sensors and actuators, solar cells and data storage, optics and photonics, medical and biological applications, tissue engineering and biomaterials, and functional nanocomposites.

Carbon nanotubes and graphene are of particular interest in the field of polymer nanocomposites due to their exceptional thermal and mechanical properties, and important efforts have been devoted to find alternative routes for reducing the cost of production of such peculiar fillers and solve the processing conditions to achieve efficient dispersion-distribution and orientation of such nanofillers within various polymer matrixes.

Graphene is a one-atom-thick planar layer of carbon atoms that are self-assembled in a honeycomb-type 2D lattice [1], where each atom of carbon is linked to three other carbon neighbors. Conversely, to diamond, where the tetravalent carbon atoms are bonded in hybridization sp^3 (four neighbors), in graphene the carbon atoms are bonded in hybridization sp^2 (three neighbors), living a nearly free delocalized electron that lies in an orbital perpendicular to the carbon plan. The structure can be pictured as a flat sheet of carbon with π -type electrons above it. This peculiar structure confers to graphene remarkable properties in terms of ballistic mobility of charge carriers (from tens to hundreds $\text{cm}^2\text{V}^{-1}\text{s}^{-1}$) [2] and thus very high electrical conductivity ($\approx 2.10^5$ S/m) [3] and extremely low resistivity (theoretically of about

Correspondence to: Abou el Kacem Qaiss; e-mail: a.qaiss@mascir.com
Contract grant sponsors: Moroccan Foundation for Advanced Science, Innovation and Research (MAsCIR) and Hassan II Academy of Science and Technology.
DOI 10.1002/pc.22198
Published online in Wiley Online Library (wileyonlinelibrary.com).
© 2012 Society of Plastics Engineers

$10^{-6} \Omega\text{-cm}$, which is lower than silver and the lowest resistivity known today at room temperature), with a zero-gap feature (the valence and the conductive bands meet at the same points), and both electrons and holes behave in a zero-mass-like relativistic particles with quantum Hall effects [4]. Graphene can also be stretched at an elongation of approximately 20% of its initial length and has exceptional thermal and mechanical properties with a fracture strength of about 120 GPa and an axial Young modulus of ~ 1 TPa [5], a thermal conductivity of about $5000 \text{ W m}^{-1} \text{ K}^{-1}$ [6], and a theoretical specific area of more than $2500 \text{ m}^2 \text{ g}^{-1}$ [7]. These extraordinary properties make of graphene a unique material for many applications such as super capacitors, batteries, sensors, hydrogen storage, solar cells, transistors, spintronics [8–10], and also as filler for making functional nanocomposites with various synergetic properties [11, 12].

Several methods have been reported to produce multiple or individual graphene nanosheets [13, 14]. In top-down processes, graphene nanosheets (GNs) can be produced by intercalation/exfoliation of graphite or graphite oxide (GO). However, starting from the bulk graphite, GNs can be made by micromechanical cleavage [1], direct exfoliation via sonication in the presence of solvents [15], electrochemical exfoliation assisted with ionic liquids [16], and through dissolution in superacids [17].

Conversely, GO is commonly used as a starting material to produce GNs. GO is produced by oxidation of graphite via one of the well-known methods developed by Brodie [18], Staudenmaier [19], and Hummers [20]. Graphene oxide can be obtained by simple sonication of dispersed GO in water solution; it is electrically insulator and thermally unstable due to the presence of oxygen-containing groups in both sides of graphene layers formed during the oxidation processes of graphite [21]. The chemistry of graphene oxide is detailed in Ref. 22. To restore electric conductivity and thermal stability of graphene oxide sheets, effective approaches to remove these functional groups are required. To reduce the graphene oxide sheets back to graphene, several approaches have been developed including thermal reduction [23, 24], ultraviolet irradiation [25] and chemical reduction using agents such as hydrazine hydrate [21], dimethylhydrazine [11], hydroquinone [26], sodium borohydride [27], sulfur-containing compounds [28], and Fe reduction [29].

Because of their large specific area, high-aspect ratio, and their intrinsic properties, the dispersion of the graphene sheets in polymer matrices is expected to lead to functional and structural nanocomposites with enhanced properties, provided good control of the interfacial properties and their dispersion-distribution and orientation within the polymer host matrix. Despite these expected properties, graphene-based polymer nanocomposites were definitely less studied when compared with nanocomposites filled with carbon nanotubes and clay, leaving plenty of room for work in this peculiar field.

Some studies on graphene-polymer nanocomposites prepared by conventional techniques, such as solution

mixing, melt blending, and in situ polymerization, revealed significant improvements in electrical conductivity [11], thermal [30] and mechanical [31] properties, and gas barrier properties [32]. Studying the properties of polystyrene-graphene nanocomposites, Stankovich et al. [11] showed that a concentration of graphene as low as 0.1 vol% was enough to achieve the electrical percolation threshold with a maximum conductivity of 0.1 S/m. These results are comparable to those obtained with CNTs-based nanocomposites [33, 34]. Ramanathan et al. [12] have reported an increase in the glass transition temperature of over 40°C upon addition of 1 wt% of thermally reduced graphene to polyacrylonitrile, whereas an increase of nearly 30°C was observed with only 0.05wt% of graphene in PMMA. Mechanical properties have also been found to be enhanced with 80% increase in Young modulus and 20% in tensile strength upon addition of 1 wt% of functionalized graphene to PMMA [12]. More important effects on mechanical properties were found on addition of 1.8 vol% of graphene to PVA, with an increase of 150% in tensile strength and close to a 10-fold increase in the Young modulus [31].

One of the challenges in the field of graphene-based nanocomposites is to disperse graphene in hydrophobic low cost-commodity polymers such as polyolefins (polypropylene [PP] and polyethylene). Only few works have been reported about PP/graphite derivatives nanocomposites, and these were mainly obtained by solid-state shear pulverization (Wakabayashi et al. [35]) and by in situ Ziegler-Natta polymerization [36].

Of great importance is the ease in obtaining GNs in powdery form or as a colloidal solution. This allows the use of conventional processing techniques to achieve low cost manufacturing of graphene-based polymer nanocomposites. Compared to in situ polymerization and solution blending method, melt mixing using commercial polymers, and classical compounding systems such as microextruder are very attractive, especially in the case of polyolefins as this approach provides many degrees of freedom with regard to the selection of polymer grades and choice of GNs loading [37].

We present here a melt-mixing method for obtaining PP/graphene nanocomposites that offers the possibility of producing large scale quantities, while using classical processing methods such as extrusion. Thermal, mechanical and rheological properties of the obtained nanocomposites are reported and discussed in terms of morphology and the state of dispersion and distribution of the GNs as assessed by spectroscopic and microscopic techniques.

MATERIALS AND EXPERIMENTAL SECTION

Materials

The main materials used in this study were natural graphite powder ($<20 \mu\text{m}$, 99.99%) purchased from Sigma Aldrich and a commercial grade of PP (PP 5032E1) purchased from ExxonMobil Chemical. The

other chemical products such as concentrated sulfuric acid (H_2SO_4 , 99.99%), hydrochloric acid (HCl , 37%), sodium nitrate (NaNO_3 , $\geq 99.0\%$), potassium permanganate (KMnO_4 , 99 %), hydrogen peroxide (H_2O_2 , 30%), and hydrazine hydrate ($\text{N}_2\text{H}_4\cdot\text{H}_2\text{O}$, 80%) were purchased from Sigma-Aldrich. All the materials were used as received.

Graphene Nanosheets Synthesis

GO was prepared from natural graphite powder by chemical oxidation using the method developed by Hummers [20]. In a typical procedure, 5 g of graphite powder and 2.5 g of sodium nitrate were mixed in a three-neck flask. Concentrated sulfuric acid (130 ml) was added to the mixture and uniformly stirred in an ice bath ($\sim 0^\circ\text{C}$). While maintaining vigorous stirring, 15 g of potassium permanganate was slowly added at a carefully controlled rate to keep the temperature below 20°C . The suspension was then stirred for 2 h after which the ice bath was removed. After heating the solution at 35°C and stirring it for 30 min, 150 ml of distilled water was slowly added to the suspension, resulting in an exothermic reaction that heated up the suspension to 95°C . Temperature was controlled at 95°C for 30 min under stirring to complete the reaction, after which the solution was diluted with 400 ml of distilled water. The solution was treated with a 30% H_2O_2 solution (5 ml) to reduce residual permanganate into soluble manganese ions until the gas evolution ceased. The cooled mixture was filtered, resulting in a yellow-brown filter cake and then washed with a 37% HCl solution to remove residues, followed by several washings with distilled water. GO was obtained by centrifugation, and the precipitate was dried at 60°C for 24 h.

GNs were obtained by chemical reduction of the graphene oxide. GO in powder form was homogeneously dispersed in distilled water, followed by sonication for 1 h allowing the exfoliation of GO into individual graphene oxide nanosheets. During this operation, it was noted that the GO dispersion gradually transformed into a yellow-brown solution during which the GO powder was transformed into GO nanosheets. Hydrazine hydrate was then added, and the solution was heated at 100°C under a water-cooled condenser for 24 h. The resulting product was isolated by filtration, washed with water and methanol several times, and dried at 80°C for 24 h, yielding GNs. Figure 1 presents the photographs of aqueous dispersions of GO before and after being reduced by hydrazine hydrate. The picture of GO before chemical reduction was taken 4 weeks after ultrasonication treatment, showing a strong stability of graphene oxide sheets in water. The picture of GNs dispersion was taken immediately after reduction process.

Nanocomposites Preparation

PP nanocomposites with various contents of GNs (0.2, 0.5, 1.0, 1.5, 2, and 3 wt%) were prepared via melt-com-



FIG. 1. Photographs of aqueous dispersions of GO before (a) and after (b) being reduced by hydrazine hydrate. [Color figure can be viewed in the online issue, which is available at wileyonlinelibrary.com.]

pounding, using a minilab twin-screw mixer (Haake Mini-lab II). Before mixing, PP and GNs were kept in an oven at 70°C several days. The components were then mixed for 10 minutes at 200°C and at a screw speed of 100 rpm. Samples for properties characterization were prepared by hot-compression molding using Carver hot press at 200°C . As reference, neat PP samples were also similarly processed for property studies.

It is to be noted that the weight fractions were transformed to volume fractions by considering the density of GNs equal to that of pristine graphite (2.28 g/cm^3) [38] and that of PP with 51% crystallinity equal to 0.901 g/cm^3 (the density of amorphous PP is equal to $\rho_{\text{Amorph}} = 0.855\text{ g/cm}^3$ and that of crystalline PP is equal to $\rho_{\text{Crist}} = 0.946\text{ g/cm}^3$).

$$\phi_{\text{GNs}} = \frac{\text{Wt}_{\text{GNs}}}{\text{Wt}_{\text{GNs}}(1 - \rho_{\text{GNs}}/\rho_{\text{PP}}) + \rho_{\text{GNs}}/\rho_{\text{PP}}}$$

where ϕ_{GNs} and Wt_{GNs} are the volume and mass fractions of GNs, respectively. ρ_{PP} and ρ_{GNs} are the densities of PP matrix (0.901 g/cm^3) and GNs (2.28 g/cm^3), respectively. Then, the volume fractions of GNs incorporated into the PP matrix can be obtained as 0.08, 0.2, 0.4, 0.6, 0.8, and 1.2 vol%.

Characterizations and Measurements

Wide-angle X-ray diffraction characterization of the graphite derivatives and the nanocomposites samples were carried out on Bruker D8 Discover, using the $\text{Cu-K}\alpha$ radiation ($\lambda = 1.54184\text{ nm}$). Tapping mode Atomic Force

Microscopy (AFM) analyses were carried out using Veeco Dimension ICON equipment. Samples for AFM images were prepared by depositing a dispersed of as-prepared GO (intercalated graphite) and chemically reduced graphene sheets solution onto a freshly cleaved mica surface and allowing them to dry in air. Fourier transforms infrared (FTIR) spectra of the graphene oxide derivatives were recorded using ABB Bomem FTLA 2000. Thermogravimetric analyses (TGA) of the samples were carried out using a Q500 system from TA Instrument by heating the samples from 25 to 1,000°C at a heating rate of 5°C·min⁻¹. Analyses of the nanocomposites samples were carried out under nitrogen over a temperature range of 25–600°C at a ramp rate of 10°C min⁻¹. Differential Scanning Calorimetry (DSC) measurements of the nanocomposites were carried out under nitrogen gas from –40 to 200°C using a DSC-Q100 from TA Instrument. To remove their thermal history, the samples were first heated to 200°C at a rate of 10°C min⁻¹ and kept at this temperature for 5 min, after which they were cooled to –40°C. Cooling and heating were performed at the same rate of 10°C min⁻¹. Morphology of the samples was characterized by scanning electron microscopy using a JEOL JSM-5500 at an acceleration voltage of 15 kV.

Tensile tests were performed using an Instron 8821S tensiometer according to ISO 527-2 procedure, using dog-bone-shaped specimens with a gauge length of 25 mm, a width of 5 mm, and a thickness of 2 mm. The stretching tests were performed at room temperature at 10 mm min⁻¹. All tests were carried out on a minimum of five samples, and the reported results are average values. Dynamic rheological measurements were performed using a strain-controlled rotational rheometer (ARES-LS, Rheometric Instruments). The measurements were carried out at 200°C under small amplitude oscillatory shear mode using parallel plate geometry (25 mm diameter). The 1-mm-thick sample disks were molded using the same conditions as those for the tensile test samples. Frequency sweeps ranging from 100 to 0.01 rad/s were applied at a strain of 2.5%, for which the materials exhibit a linear viscoelastic behavior as verified by previous strain sweeps. Specimens were allowed to equilibrate for ~10 min before each frequency sweep run.

RESULTS AND DISCUSSION

Graphene Nanosheets Characterization

Production of individual graphene sheets from graphite by the graphene oxide route was confirmed through the use of X-ray diffraction (XRD), AFM, FTIR, and TGA. Figure 2 shows the XRD patterns obtained from pristine graphite, GO, and GNs. The X-ray spectrum of the graphite powder shows the hexagonal structure along the (200) orientation, as revealed by the single peak at $2\theta = 26.23^\circ$ corresponding to a ~0.34 nm spacing between the graph-

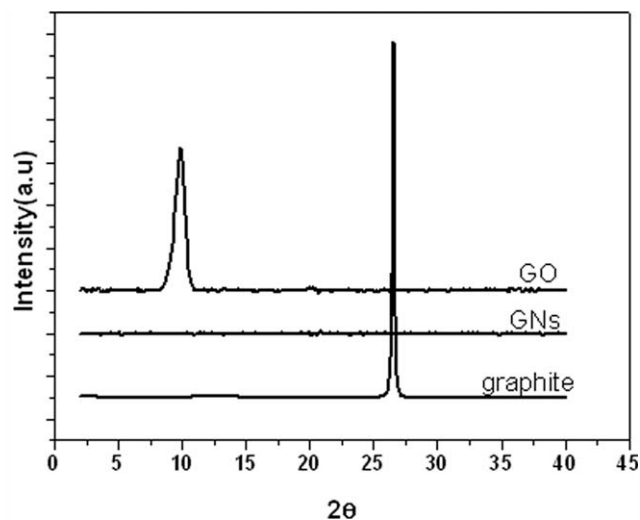


FIG. 2. XRD pattern of pristine graphite, graphite oxide (GO), and chemically reduced graphene oxide (GNs).

ite planes. During oxidation of graphite into graphene oxide, an increase in the interplane spacing is observed due to the formation of oxygen-containing groups intercalated within the layered structure, with the 2θ peak shifting from 26.23° to $\approx 10^\circ$. This corresponds to an interplane spacing of 0.9 nm, wider than the previous 0.34 nm value. In addition to the shift to lower angle, the characteristic peak is broadened due to reduction in average crystallites size. The absence of any secondary peaks indicates a complete oxidation of the graphite into GO. The high level exfoliation and chemical reduction of GO into GNs was confirmed by XRD, as the resulting spectrum is devoided of any characteristic peak, thus confirming the removal of the layered periodic structure.

Before exfoliating of GO into graphene oxide sheets via ultrasonication treatment in water, the as-intercalated graphite by oxygen-containing groups was visualized using AFM measurement. Figure 3 shows a typical tapping mode AFM image of nonexfoliated GO deposited onto a mica substrate from an aqueous dispersion. After oxidation of graphite into GO, an increase in the interplane spacing can be observed due to the formation of oxygen-containing groups. It is clear that the graphene oxide sheets are still arranged together, and the graphite structure is still present due to strong van der Waals interactions between graphite plans. Upon exfoliation, the layered structure is destroyed. Figure 3 shows the morphology and thickness of as-exfoliated graphene sheets; it is to be noted that the sheets have a different lateral dimensions, and they are stacked with each other. The line profiles shown in Fig. 3 indicate an average thickness of ~1 nm, which is similar to earlier results of the literature [3, 21].

FTIR analyses revealed that the mixture of potassium permanganate, sulfuric acid and sodium nitrate used during the chemical oxidation of graphite results in the formation of carboxyl, epoxide, and peroxide functions on both side of each graphite plane, as well as water mole-

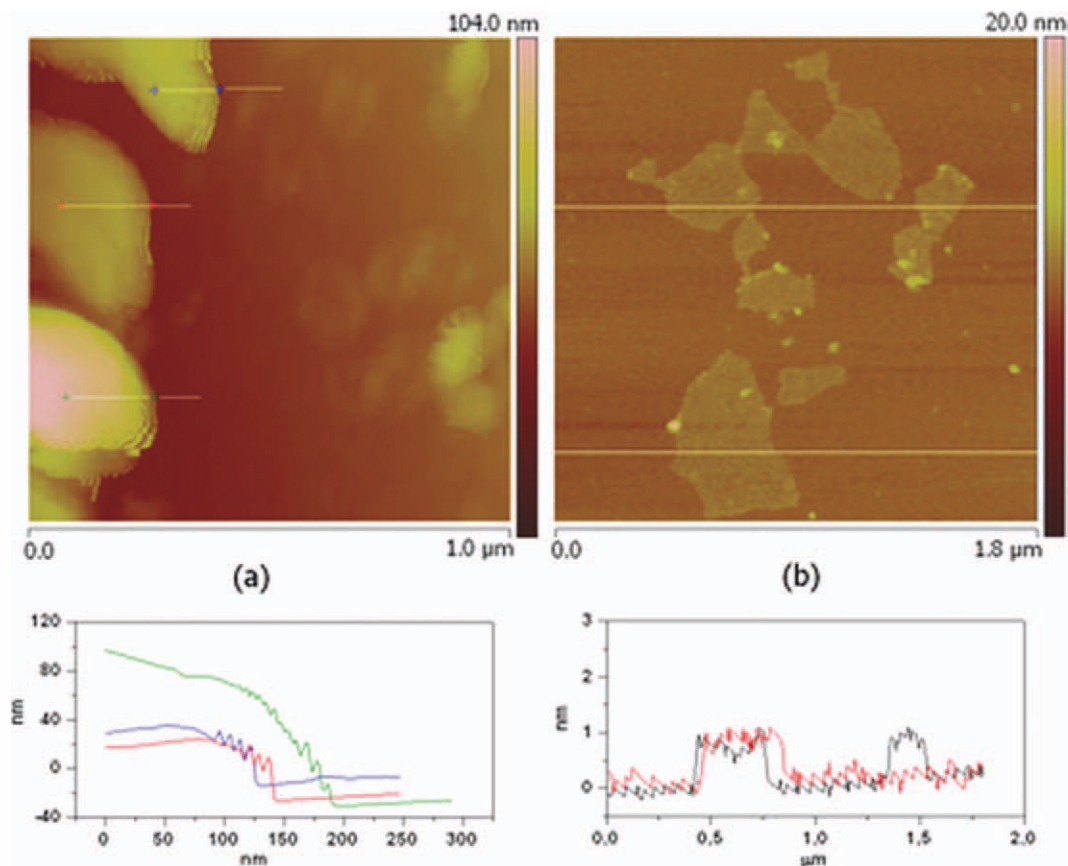


FIG. 3. Tapping mode AFM image of (a) nonexfoliated graphite oxide (GO) and (b) exfoliated GNs deposited on mica surface and their corresponding height profiles (under images) along the indicated straight lines. [Color figure can be viewed in the online issue, which is available at wileyonlinelibrary.com.]

cules [39] (Fig. 4). The existence of several bands in the spectrum of graphene oxide confirms the presence of oxygen-containing groups. The bands at $3,680\text{ cm}^{-1}$ and $1,410\text{--}1,280\text{ cm}^{-1}$ are attributed respectively to the stretching and in-plane deformation of the O—H bonds in hydroxyl groups. The intense peaks between $1,600$ and

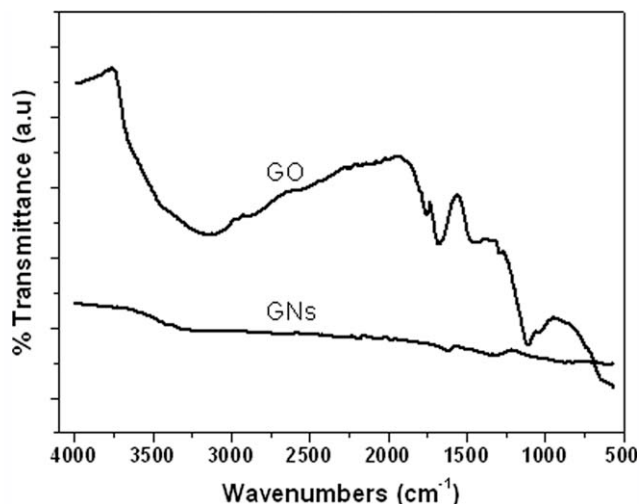


FIG. 4. FTIR spectra of graphite oxide (GO) and chemically reduced graphene oxide (GNs).

$1,800\text{ cm}^{-1}$ can be assigned to the stretching vibration of C=O in carboxyl groups, while the bands at $1,000$ and $1,150\text{ cm}^{-1}$ are assigned to C=O in epoxide. Finally, several C—H bands are found around $2,000\text{--}3,340\text{ cm}^{-1}$. The intense peak at $3,800\text{ cm}^{-1}$ has been attributed to H_2O molecules, indicating that the GO was intercalated by a certain amount of water [40]. The FTIR spectrum obtained after chemical reduction is devoided of any noticeable absorption bands, indicating that H_2O molecules and most of the oxygen-containing groups were totally removed after the chemical reduction of GO (Fig. 4). These findings are in good agreement with the results of the literature, confirming the complete reduction of GO in graphene [37, 40–42].

The thermal stability of GO and GNs in air was studied by TGA, are compared with that of the pristine graphite (Fig. 5). Combustion driven thermal degradation of graphite starts at around 650°C , leading to the formation of carbon dioxide (90%) [26]. The thermally unstable GO decomposes following a three steps process. In the first step, residual water is lost in the initial stage of heating (100°C , 10%). The second step begins at around 190°C , where a considerable weight loss (80%) occurs corresponding to the decomposition of the oxygen-containing groups. The final weight loss (5%) at 550°C is attributed

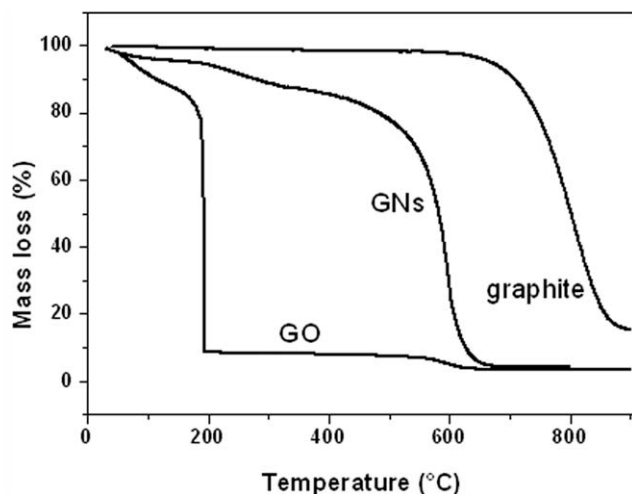


FIG. 5. TGA curves of pristine natural graphite, graphite oxide (GO), and chemically reduced graphene oxide (GNs).

to the oxidation of carbon [21, 26]. The reduced graphene oxide shows a strong thermal stability, with only small weight loss (5%) found at about 300°C, revealing the oxidation of amorphous carbon in the sample [21, 30].

GNs-Filled Polypropylene Nanocomposites Characterizations

X-Ray Diffraction. GNs-filled PP nanocomposites were analyzed by XRD to evaluate the effects of GNs on the crystalline structure of the neat PP and to check the formation of eventual GNs rearrangements (Fig. 6). This last point is critical because the strong Vander-Waals interactions between individual graphene platelets will tend to form irreversible layered structure and consequently will reduce the properties of the nanocomposite. The absence of a peak related to the graphitic structure indicates that GNs were successfully dispersed. But the addition of GNs also affected the crystalline structure of the host matrix. Neat PP exhibits α - and β -crystallization forms, with peaks at $2\theta = 14.1, 16.9, 21.2, 21.9, 25.5,$ and 28.6 corresponding respectively to the (110), (040), (130), (111), (131) + (041), (150) + (060), and (220) planes of the α -crystal form [43]. The low intensity peak at $2\theta = 16.2$ corresponds to the (300) plane of the β -crystal form of PP [44]. The addition of GNs to the PP matrix induces changes in its crystals conformation, resulting in the complete disappearance of the β -crystal form to become α -PP. This result is consistent with previous study on PP/SWCNT and PP/MWCNT nanocomposites [45, 46].

Scanning Electron Microscopy. Scanning electron microscopy images of nanocomposites containing 1, 1.5, and 2 wt% of GNs are reported in Fig. 7. A reasonable uniform dispersion of GNs in the polymer matrix can be observed, with however the presence of some aggregates at the nanocomposite surfaces. This indicates to some

degree of good interactions between GNs and the polymer matrix.

Crystallization and Melting Properties. In general, the properties of semicrystalline thermoplastic materials are strongly related to their internal microstructure and crystallinity, particularly the mechanical properties and thermal stability. Therefore, the crystallization and melting behaviors of PP matrix was studied under nonisothermal conditions as function of GNs loading.

Crystallization and melting curves from second heating and first cooling cycles (DSC) for neat PP and its nanocomposites are reported in Fig. 8a and b. From these curves, the associated thermal parameters of crystallization (T_c) and melting (T_m) temperatures, crystallization enthalpy (ΔH_c), heat of melting (ΔH_m), and the percentage of crystallinity (X_c) were extracted and presented in Table 1. The relative X_c was determined from the melting curves with the following expression: $X_c = (\Delta H_m / (1 - x) \Delta H_0) \times 100$, where ΔH_m is the melting heat of samples, ΔH_0 is the theoretical value of the melting heat for a 100% crystalline PP which is 165 J g^{-1} [47], and x is the weight fraction of GNs in the sample. Figure 8a shows the crystallization thermograms of neat PP and PP filled with GNs at a cooling rate of $10^\circ\text{C min}^{-1}$. For neat PP, the crystallization temperature, T_c , is observed at 116.9°C , whereas for PP/GNs T_c increases by about 5°C and the crystallinity increases by about 17% upon addition of GNs. The increase in T_c indicates a heterogeneous nucleation effect of GNs which facilitate the crystallization of PP during cooling [48]. Such increase stabilizes for concentrations ranging between 0.5 and 1 wt% (0.2 and 0.4 vol%) which presumes that the percolation threshold concentration lies between these two values. This point will be discussed in the rheology section.

Figure 8b shows the DSC melting curves at a heating rate of 10°C/min . The results show two important differ-

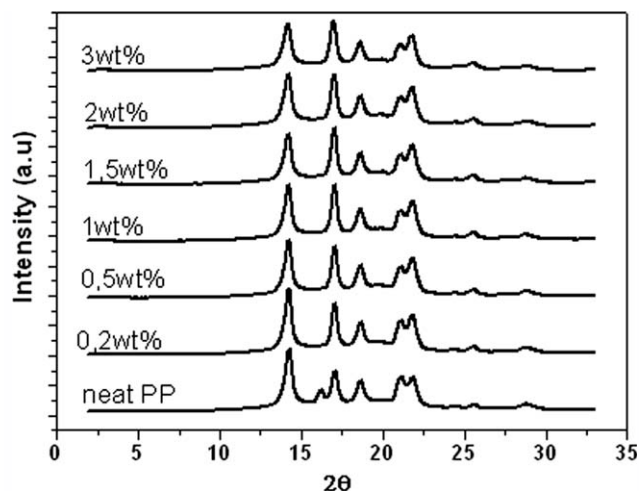


FIG. 6. XRD patterns of neat PP and its nanocomposites with effective GNs contents of 0.2, 0.5, 1.0, 1.5, 2.0, and 3.0 wt%.

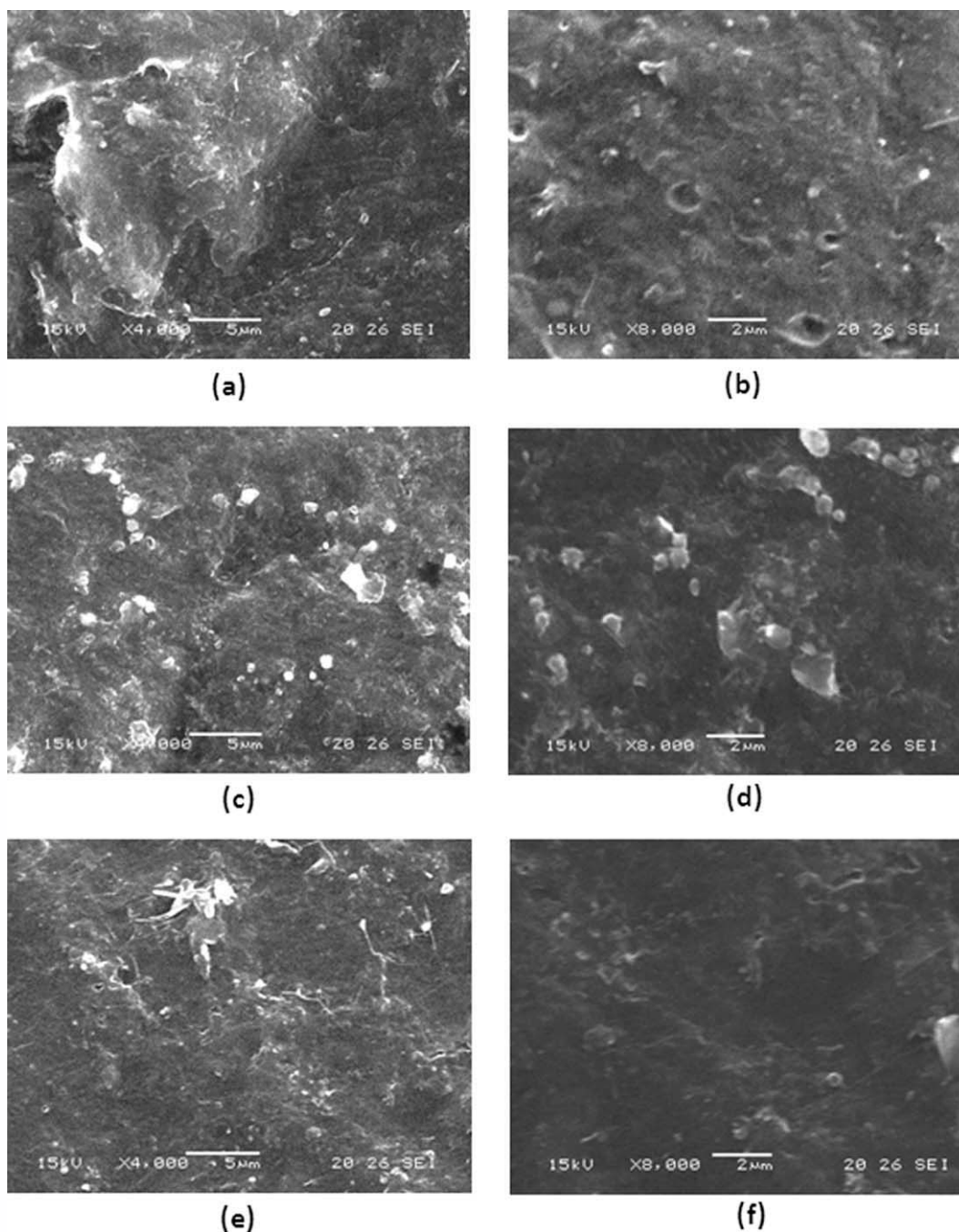


FIG. 7. Low- (left) and high- (right) magnification SEM images of PP nanocomposites containing (a) and (b) 1 wt%; (c) and (d) 1.5 wt%; (e) and (f) 2 wt% of GNs content.

ences between neat PP and its nanocomposites. First, the neat PP shows two main melting peaks, while all the nanocomposites containing GNs exhibit only one peak. The second difference is the increase in the melting temperature with increasing GNs content. For neat PP, the peak at 164.9°C is attributed to the melting of α -crystals, the most common monoclinic crystal structure of PP, whereas the peak at 147.5°C is attributed to the melting of β -crystals. For PP nanocomposites, the DSC results (Table 1) confirm that no β -crystalline structure is present, which is in-line with the XRD results (Fig. 6).

From Fig. 8b, neat PP exhibits a melting temperature at 164.9°C, while in all PP-GNs nanocomposites there is a slight shift up to 6°C in the melting point (Table 1).

The increase in crystallization enthalpy for the nanocomposites is linked to the increased degree of crystallization of neat PP as the dispersed filler act a nucleating agent for PP crystallization. Changes in the crystallization characteristics of PP by the addition of GNs are of crucial importance for understanding the mechanical properties of these nanocomposites.

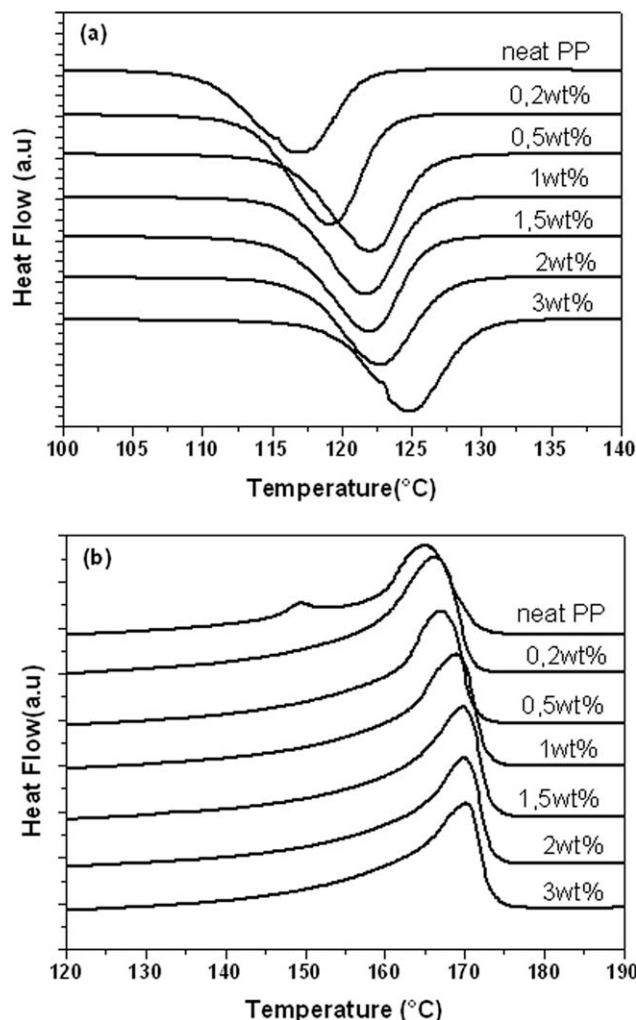


FIG. 8. (a) Crystallization thermograms (first cooling cycle) and (b) melting thermograms (second heating cycle) of neat PP and its nanocomposites with various GNs contents of 0.2, 0.5, 1.0, 1.5, 2.0, and 3.0 wt%. At a $10^{\circ}\text{C min}^{-1}$ cooling rate.

Thermal Stability of Nanocomposites. Thermal stability is very important for polymeric materials as it is often the limiting factor both in processing and in end-use applications. Thermal degradation of PP and PP nanocomposites with different weight fractions of GNs was deter-

TABLE 1. Summarized results of DSC analysis of PP and its nanocomposites with different GNs content.

GNs content		DSC				
Wt%	Vol%	T_c (°C)	ΔH_{cryst} (J/g)	T_m (°C)	ΔH_{melt} (J/g)	X_c (%)
0	—	116.90	97.14	164.88 ^a	90.15	51.04
0.2	0.08	119.09	97.68	166.14	104.16	63.25
0.5	0.2	122.07	101.52	167.05	97.80	59.57
1	0.4	121.07	103.32	168.87	97.50	59.68
1.5	0.6	121.87	103.44	169.72	97.68	60.10
2	0.8	122.64	103.23	169.91	96.42	59.62
3	1.2	124.85	104.82	170.12	95.52	59.68

^a It is attributed to the melting temperature of α -crystals.

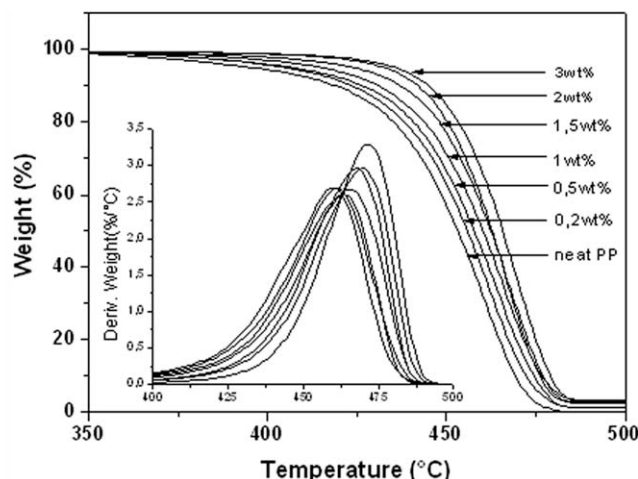


FIG. 9. TGA and DTG thermograms of neat PP and its nanocomposites with various GNs contents of 0.2, 0.5, 1.0, 1.5, 2.0, and 3.0 wt%.

mined from the weight loss during heating. In Fig. 9, the weight loss (TGA) and derivative weight loss (DTG) curves are presented for a heating rate of 10°C/min under nitrogen atmosphere. From these curves, the temperature for 5 and 15% weight loss ($T_{5\%}$ and $T_{15\%}$) and the maximum decomposition temperature (T_{max}) were extracted and the results are summarized in Table 2. Because the as-prepared GNs exhibit a good thermal stability in the range where polymer processing is performed, they can be incorporated into a PP matrix by melt blending without any noticeable degradation. Thermal degradation of the neat PP and its nanocomposites occurs as a single step process, with a maximum decomposition temperature at around 460°C , while the values at a weight loss of 5 and 15% for neat PP are at 396 and 428°C , respectively. The addition of GNs increases the thermal stability by around 40°C for $T_{5\%}$, 20°C for $T_{15\%}$, and 10°C for T_{max} . From these data, it is clear that the incorporation of GNs nanosheets leads to a noticeable increase in PP thermal stability at the initial stage of degradation (Table 3). The improvement in the resistance to thermal degradation can be attributed to the hindered diffusion of volatile decomposition products within the nanocomposites, and it is strongly dependent on the nanosheets-polymer chains interactions. The GNs content shows some effects on the

TABLE 2. Summarized results of TGA analysis ($T_{5\%}$, $T_{15\%}$, and T_{max}) of PP and its nanocomposites with different GNs content.

GNs content		TGA		DTG
Wt%	Vol%	$T_{5\%}$ (°C)	$T_{15\%}$ (°C)	T_{max} (°C)
0	—	396.15	428.50	460.13
0.2	0.08	405.32	431.73	461.53
0.5	0.2	407.34	434.82	462.15
1	0.4	415.14	437.67	465.23
1.5	0.6	424.83	443.11	467.98
2	0.8	433.64	446.52	469.37
3	1.2	436.57	450.00	470.18

TABLE 3. Summarized results of mechanical properties and its % increase of neat PP and its nanocomposites with different GNs content.

GNs content		Young's	%	Tensile	%	Elongation
Wt%	Vol%	Modulus, E (Mpa)	increase of E	strength, σ (Mpa)	increase of σ	at break (%)
0	—	1154.48	—	33.98	—	279.91
0.2	0.08	1252.21	14.66	37.58	10.59	36.33
0.5	0.2	1576.96	36.59	38.81	14.21	28.34
1	0.4	1785.33	54.64	43.93	29.28	27.49
1.5	0.6	1888.27	63.55	51.37	51.17	26.28
2	0.8	2040.04	76.70	56.17	65.30	21.71
3	1.2	2314.61	100.48	61.57	81.19	19.09

The values were calculated from typical stress-strain curves.

mechanism and reaction kinetics for concentrations higher than 1.5 wt%, as the shape of the DTG peak broadens past this point. Such important increases widen the spectrum of application of PP, whenever thermal stability is a key factor.

Mechanical Properties. The large aspect ratio and very high Young's modulus of GNs should have a significant reinforcement impact on mechanical properties. Dispersion-exfoliation and homogenous distribution of GNs along with the favorable interfacial interactions between GNs and the polymer matrix are the key points needed to achieve polymer nanocomposites with enhanced final properties.

The mechanical behavior is strongly dependent on the crystallization characteristics of polymer materials [49] and the induced of crystallization with the increase in the loading of the nanofillers [49]. This effect of crystallization was observed not only for PP, but for other polymer matrices such as PVA [50]. Thermally reduced graphene oxide nanosheets were already used as reinforcing fillers to enhance the mechanical properties of polymer materials with significant improvements in properties [12, 38, 51]. The results obtained in this work by incorporating GNs to PP matrix show significant improvements in mechanical properties. In fact, typical stress-strain curves obtained by uniaxial tensile testing of the PP matrix and its GNs nanocomposites are presented in Fig. 10a. The extracted values of the Young modulus, tensile strength and elongation at break and the percent of increase are summarized in Tab.3 and they are plotted in Fig. 10b and c as a function of GNs content. The results show that the Young modulus and tensile strength increase significantly with increasing GNs content due to their high mechanical strength. The addition of only 1 wt% (0.4 vol%) of GNs results in an increase of the Young modulus and the tensile strength of about 64 and 54%, respectively, as compared with neat PP values. As the loading of GNs increases to 3 wt% (1.2 vol%), the Young modulus and tensile strength of PP/GNs nanocomposites show substantial increase of about 100 and 81%, respectively. As can be expected for any filled polymer, the addition of GNs

results in a dramatic decrease in the elongation at break, even when GNs loading is as low as 0.2–0.5 wt% (Fig. 10c). The improvement of mechanical properties can be attributed to a large aspect ratio and high intrinsic mechanical characteristics of GNs as well as the relatively strong interfacial interaction between GNs and PP, leading to a better interfacial stress transfer efficiency, which restricts the movement of the polymer chains.

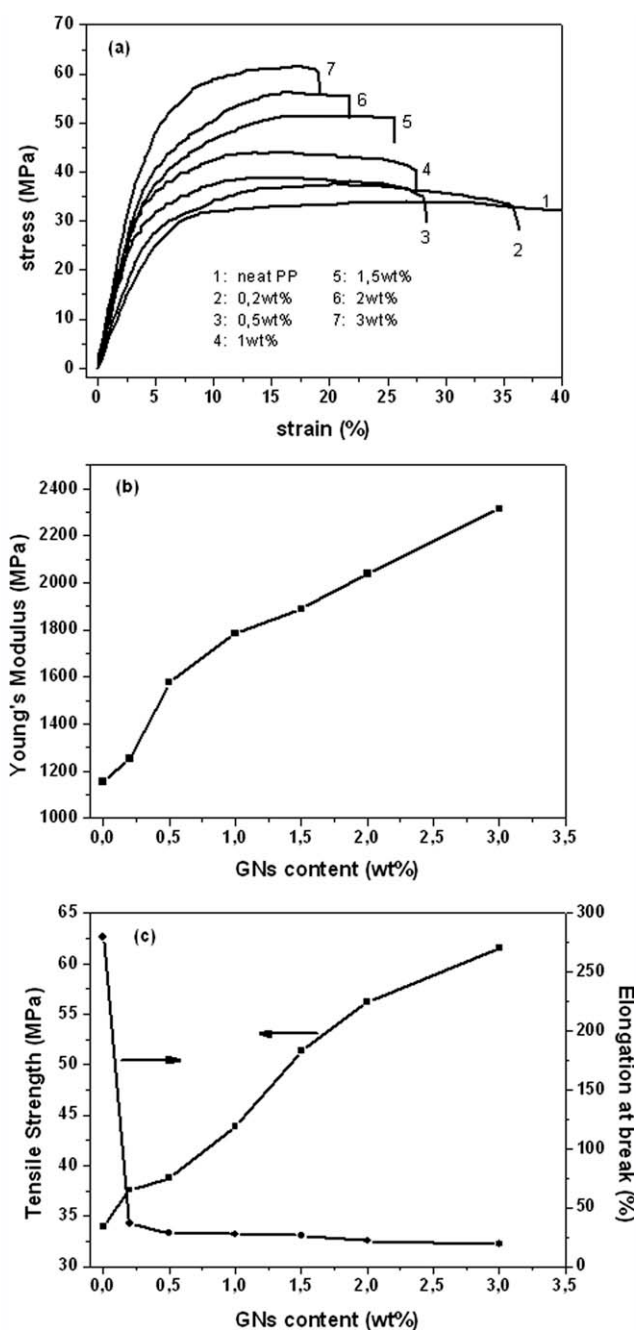


FIG. 10. (a) Typical stress-strain curves of the neat PP and its nanocomposites at indicated GNs contents (crosshead speed set at 10 mm/min), (b) Young's modulus, and (c) tensile strength and elongation at break of GNs-filled PP nanocomposites as a function of GNs content.

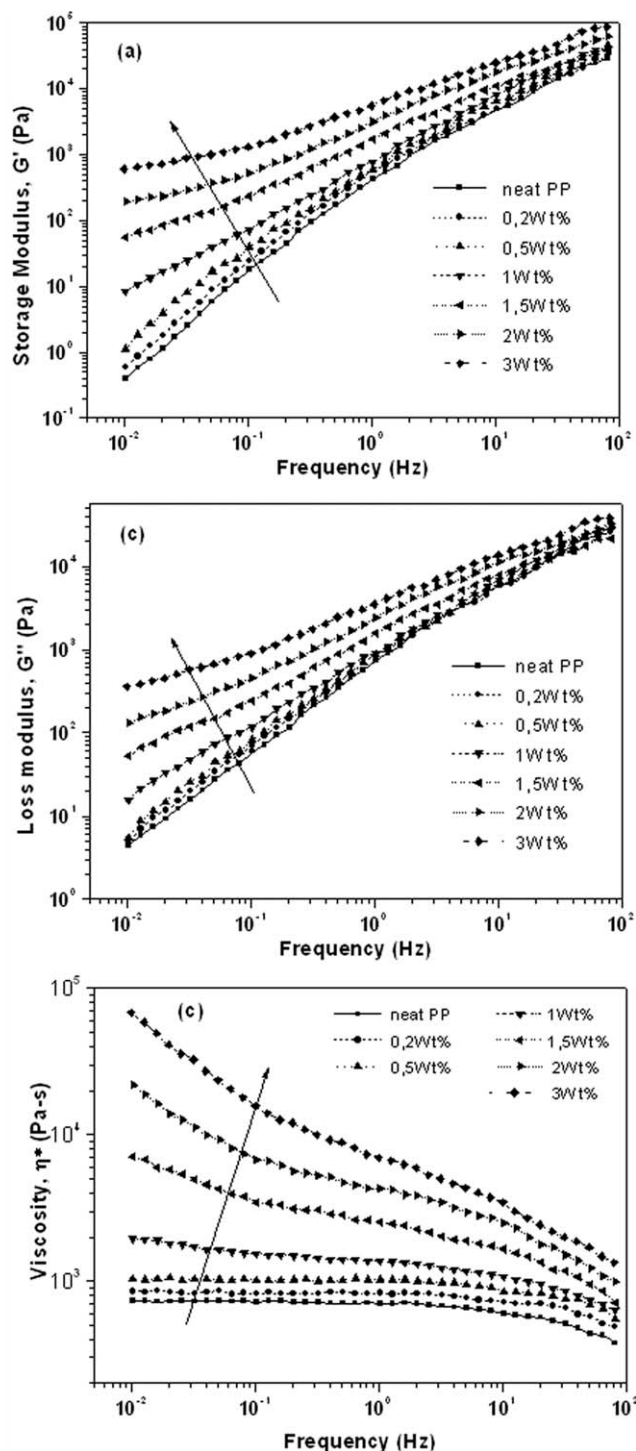


FIG. 11. (a) Storage modulus (G'), (b) loss modulus (G''), and (c) complex viscosity (η^*) vs. frequency of neat PP and its nanocomposites with effective GNs contents of 0.2, 0.5, 1.0, 1.5, 2.0, and 3.0 wt% at 200°C.

Melt Rheology. Neat and filled PP with various concentrations of GNs were submitted to small amplitude oscillatory shear flow at 200°C in the frequency range 10^{-2} to 10^2 Hz. The measured dynamic storage modulus, G' , and loss modulus, G'' , and the dynamic viscosity, η^* , are reported in Fig. 11a–c, respectively. PP shows the classical polymer melt behavior with G' decreasing with

lowering of frequency and a clear terminal zone in the low frequency range. GNs-filled PP nanocomposites show an increase in G' and viscosity with GNs loading and the appearance of a pseudo-plateau in the low frequency region for concentrations larger than 0.5 wt%. For 0.2 and 0.5 wt% which are equivalent to 0.08 and 0.2 vol%, respectively, both G' and η^* increase slightly and show a terminal zone behavior (Newtonian behavior for viscosity and Maxwellian behavior for the dynamic moduli), whereas for concentration higher than 0.5 wt%, both viscosity and G' level off and deviate from the terminal zone behavior with the appearance of a pseudo-plateau on G' having a magnitude that increases with the GNs loading. This has to be connected to the formation of a three-dimensional network of GNs with a density increasing with the concentration of GNs. This apparently occurs at a percolation threshold that lies between 0.5 and 1 wt% (0.2 and 0.4 vol%).

Evidence of the formation of a solid-like network of percolated GNs nanosheets can also be deduced from the comparison of the G' and G'' moduli as function of GNs content at different frequencies. Figure 12a shows the

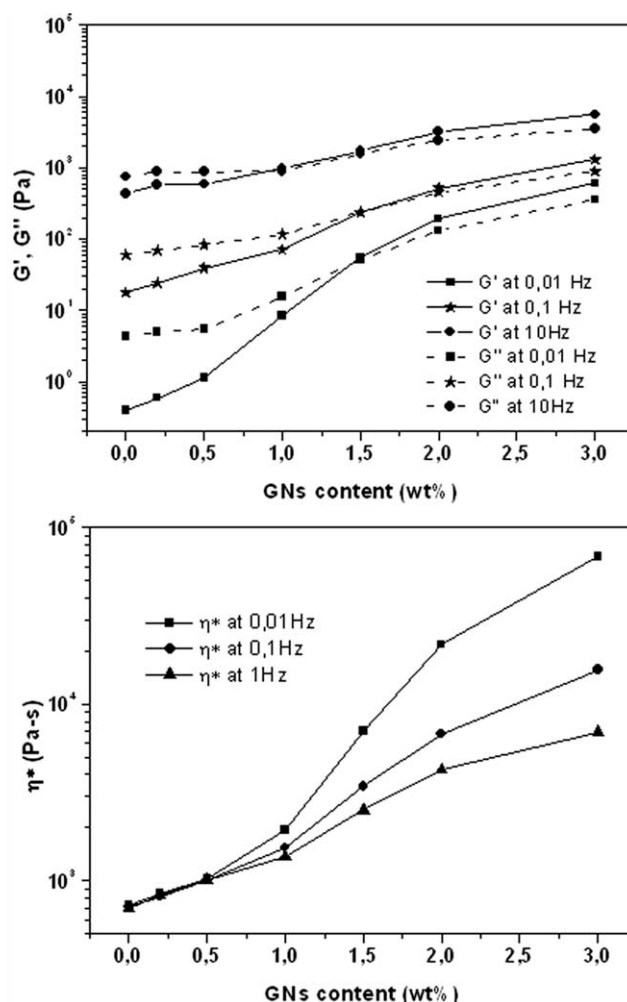


FIG. 12. (a) Storage modulus (G') and loss modulus (G'') and (b) complex viscosity (η^*) at 0.01, 0.1, and 1 Hz of GNs-filled PP nanocomposites as a function of GNs content.

storage (G') and loss (G'') moduli against GNs content for frequencies of 0.01, 0.1, and 1 Hz. While the values of both G' and G'' increase with increasing GNs content, a clear viscoelastic transition can be observed throughout the studied range of GNs concentrations. For neat PP and PP nanocomposites with low GNs content (0.2 and 0.5 wt %), the viscous behavior is dominant at low frequency ($G'' > G'$, $\tan \delta > 1$), while the elastic behavior ($G' > G''$, plateau in G' at low frequency) becomes dominant when GNs loading is higher than 1 wt% (0.4 vol%).

Figure 12b shows the complex shear viscosity as function of GNs loading at frequencies of 0.01, 0.1, and 1 Hz. No significant changes were observed between neat PP and its nanocomposites containing ≤ 0.5 wt% of GNs, all samples exhibit a Newtonian behavior at low frequency (Fig. 11c). For nanocomposites containing ≥ 1 wt% of GNs, there is a clear increase in the complex shear viscosity with GNs content. This is accompanied by the formation of GNs networks in the PP matrix and the transition from liquid-like to solid-like viscoelastic response. Thus a GNs concentration between 0.5 and 1 wt% (0.2 and 0.4 vol%) can be regarded as rheological percolation threshold. Similar phenomena have been reported in the literature for polyolefins reinforced with functionalized CNT for which the percolation threshold was found to be between 0.5 and 0.75 wt.% [48,52–55].

CONCLUSION

Nanocomposites of PP reinforced with different amounts (0.2–3 wt%; 0.08–1.2 vol%) of chemically reduced graphene oxide nanosheets (GNs) were prepared by melt compounding using a twin-screw co-rotating extruder. Thermal and mechanical properties, as well as the melt rheology behavior of the obtained nanocomposites were compared to neat PP to evaluate the impact of GNs addition. The results have shown that the crystallinity, crystallization and melting temperatures of PP were increased as the amount of GNs was increased, indicating that the GNs acts as nucleating agents. All PP/GNs nanocomposites showed an improvement in thermal stability of PP. The PP/GNs nanocomposites also exhibited a significant improvement of mechanical properties indicating an efficient load transfer between GNs and the PP matrix. The addition of GNs in PP had also a dramatic influence on the rheological properties of the nanocomposites, especially at low frequency range where the nanocomposites switch the behavior from liquid-like to solid-like behavior for concentrations higher than the percolation threshold concentration (0.2–0.4 vol%).

REFERENCES

1. K.S. Novoselov, A.K. Geim, S.V. Morozov, D. Jiang, Y. Zhang, S.V. Dubonos, I.V. Grigorieva, and A.A. Firsov, *Science*, **306**, 666 (2004).
2. K.I. Bolotin, K.J. Sikes, Z. Jiang, M. Klima, G. Fudenberg, J. Hone, P. Kim, and H.L. Stormer, *Solid State Commun.*, **146**, 351 (2008).
3. Z.S. Wu, W. Ren, L. Gao, J. Zhao, Z. Chen, B. Liu, D. Tang, B. Yu, C. Jiang, and H.M. Cheng, *ACS Nano*, **3**, 411 (2009).
4. K.S. Novoselov, Z. Jiang, Y. Zhang, S.V. Morozov, H.L. Stormer, U. Zeitler, J.C. Maan, G.S. Boebinger, P. Kim, and A.K. Geim, *Science*, **315**, 1379 (2007).
5. C. Lee, X. Wei, J.W. Kysar, and J. Hone, *Science*, **321**, 385 (2008).
6. A.A. Balandin, S. Ghosh, W. Bao, I. Calizo, D. Teweldebrhan, F. Miao, and C.N. Lau, *Nano Lett.*, **8**, 902 (2008).
7. M.D. Stoller, S. Park, Y. Zhu, J. An, and R.S. Ruoff, *Nano Lett.*, **8**, 3498 (2008).
8. M. Terrones, A.R. Botello-Méndez, J.C. Delgado, F.L. Urías, Y.I. Vega-Cantú, R.F.J. Macías, A.L. Elías, E. Muñoz-Sandoval, A.G. Cano-Márquez, J.C. Charlier, and H. Terrones, *Nano Today*, **5**, 351 (2010).
9. C. Soldano, A. Mahmood, and E. Dujardin, *Carbon*, **48**, 2127 (2010).
10. Y. Zhu, S. Murali, W. Cai, X. Li, J.W. Suk, J.R. Potts, and R.S. Ruoff, *Adv. Mater.*, **22**, 3906 (2010).
11. S. Stankovich, D.A. Dikin, G.H.B. Dommett, K.M. Kohlhaas, E.J. Zimney, E.A. Stach, R.D. Piner, S.T. Nguyen, and R.S. Ruoff, *Nature*, **442**, 282 (2006).
12. T. Ramanathan, A.A. Abdala, S. Stankovich, D.A. Dikin, M. Herrera-Alonso, R.D. Piner, D.H. Adamson, H.C. Schniepp, X. Chen, R.S. Ruoff, S.T. Nguyen, I.A. Aksay, R.K. Prud'Homme, and L.C. Brinson, *Nat. Nanotech.*, **3**, 327 (2008).
13. H. Kim, A.A. Abdala, and C.W. Macosko, *Macromolecules*, **43**, 6515 (2010).
14. S. Park, and R.S. Ruoff, *Nat. Nanotech.*, **4**, 217 (2009).
15. A.B. Bourlinos, V. Georgakilas, R. Zboril, T.A. Steriotis, A.K. Stubos, and C. Trapalis, *Solid State Commun.*, **149**, 2172 (2009).
16. N. Liu, F. Luo, H. Wu, Y. Liu, C. Zhang, and J. Chen, *Adv. Funct. Mater.*, **18**, 1518 (2008).
17. N. Behabtu, J.R. Lomeda, M.J. Green, A.L. Higginbotham, D.V. Kosynkin, D. Tsentelovich, A.N.G. Parra-Vasquez, J. Schmidt, E. Kesselman, Y. Cohen, Y. Talmon, J.M. Tour, and M. Pasquali, *Nat. Nanotech.*, **5**, 406 (2010).
18. B.C. Brodie, *Proc. Roy. Soc. Lond.*, **149**, 249 (1859).
19. L. Staudenmaier, *Ber. Dtsch. Chem. Ges.*, **31**, 1481 (1898).
20. W.S. Hummers and R.E. Offeman, *J. Am. Chem. Soc.*, **80**, 1339 (1958).
21. S. Stankovich, D.A. Dikin, R.D. Piner, K.A. Kohlhaas, A. Kleinhammes, Y. Jia, Y. Wu, S.T. Nguyen, and R.S. Ruoff, *Carbon*, **45**, 1558 (2007).
22. D.R. Dreyer, S. Park, C.W. Bielawski, and R.S. Ruoff, *Chem. Soc. Rev.*, **39**, 228 (2010).
23. H.C. Schniepp, J.L. Li, M.J. McAllister, H. Sai, M.H. Alonso, D.H. Adamson, R.K. Prud'homme, R. Car, D.A. Saville, and I.A. Aksay, *J. Phys. Chem. B*, **110**, 8535 (2006).
24. M.J. McAllister, J.L. Li, D.H. Adamson, H.C. Schniepp, A.A. Abdala, J. Liu, M.H. Alonso, D.L. Milius, R. Car, R.K. Prud'homme, and I.A. Aksay, *Chem. Mater.*, **19**, 4396 (2007).
25. G. Williams, B. Seger, and P.V. Kamat, *ACS Nano*, **2**, 1487 (2008).

26. G. Wang, J. Yang, J. Park, X. Gou, B. Wang, H. Liu, and J. Yao, *J. Phys. Chem. C*, **112**, 8192 (2008).
27. W. Gao, L.B. Alemany, L. Ci, and P.M. Ajayan, *Nat. Chem.*, **1**, 1403 (2009).
28. W. Chen, L. Yan, and P.R. Bangal, *J. Phys. Chem. C*, **114**, 19885 (2010).
29. Z.J. Fan, W. Kai, J. Yan, T. Wei, L.J. Zhi, J. Feng, Y. Ren, L.P. Song, and F. Wei, *ACS Nano*, **5**, 191 (2011).
30. A.S. Patole, S.P. Patole, H. Kang, J.B. Yoo, T.H. Kim, and J.H. Ahn, *J. Colloid Int. Sci.*, **350**, 530 (2010).
31. X. Zhao, Q. Zhang, D. Chen, and P. Lu, *Macromolecules*, **43**, 2357 (2010).
32. H. Kim, Y. Miura, and C.W. Macosko, *Chem. Mater.*, **22**, 3441 (2010).
33. N. Grossiord, J. Loos, and C.E. Koning, *J. Mater. Chem.*, **5**, 2349 (2005).
34. D.S. McLachlan, C. Chiteme, C. Park, K.E. Wise, S.E. Lowther, P.T. Lillehei, E.J. Siochi, and J.S. Harrison, *J. Polym Sci B: Polym Phys.*, **43**, 3273 (2005).
35. K. Wakabayashi, C. Pierre, D.A. Dikin, R.S. Ruoff, T. Ramanathan, L.C. Brinson, and J.M. Torkelson, *Macromolecules*, **41**, 1905 (2008).
36. Y. Huang, Y. Qin, Y. Zhou, H. Niu, Z.Z. Yu, and J.Y. Dong, *Chem. Mater.*, **22**, 4096 (2010).
37. H.B. Zhang, W.G. Zheng, Q. Yan, Y. Yang, J.W. Wang, Z.H. Lu, G.Y. Ji, and Z.Z. Yu, *Polymer*, **51**, 1191 (2010).
38. H. Kim and C.W. Macosko, *Macromolecules*, **41**, 3317 (2008).
39. M. Acik, C. Mattevi, C. Gong, G. Lee, K. Cho, M. Chhowalla, and Y.J. Chabal, *ACS Nano*, **4**, 5861 (2010).
40. H.M. Ju, S.H. Huh, S.H. Choi, and H.L. Lee, *Mater. Lett.*, **64**, 357 (2010).
41. D.C. Marcano, D.V. Kosynkin, J.M. Berlin, A. Sinitskii, Z. Sun, A. Slesarev, L.B. Alemany, W. Lu, and J.M. Tour, *ASC Nano*, **4**, 4806 (2010).
42. P. Zhu, M. Shen, S. Xiao, and D. Zhang, *Physica B*, **406**, 498 (2011).
43. B.X. Yang, J.H. Shi, K.P. Pramoda, and S.H. Goh, *Compos. Sci. Tech.*, **68**, 2490 (2008).
44. Z. Yang, Z. Zhang, Y. Tao, and K. Mai, *Eur. Polym. J.*, **44**, 3754 (2008).
45. A.R. Bhattacharyya, T.V. Sreekumar, T. Liua, S. Kumar, L.M. Ericson, R.H. Hauge, and R.E. Smalley, *Polymer*, **44**, 2373 (2003).
46. E. Logakis, E. Pollatos, C.H. Pandis, V. Peoglos, I. Zuburtikudis, C.G. Delides, A. Vatalis, M. Gjoka, E. Syskakis, K. Viras, and P. Pissis, *Compos. Sci. Tech.*, **70**, 328 (2010).
47. J.E. Mark, *Polymer Data Handbook*, New York, Oxford University Press (1999).
48. T. McNally, P. Pötschke, P. Halley, M. Murphy, D. Martin, S.E.J. Bell, G.P. Brennan, D. Bein, P. Lemoine, and J.P. Quinn, *Polymer*, **46**, 8222 (2005).
49. J.N. Coleman, M. Cadek, R. Blake, V. Nicolosi, K. Ryan, C. Belton, A. Fonseca, J. Nagy, Y. Gun'ko, and W. Blau, *Adv. Funct. Mater.*, **14**, 791 (2004).
50. K.E. Prasad, B. Das, U. Maitra, U. Ramamurty, and C.N.R. Rao, *PNAS*, **106**, 13186 (2009).
51. H. Kim, S. Kobayashi, M.A. AbdurRahim, M.J. Zhang, A. Khusainova, M.A. Hillmyer, A.A. Abdala, and C.W. Macosko, *Polymer*, **52**, 1837 (2011).
52. J.I. Lee, S.B. Yang, and H.T. Jung, *Macromolecules*, **42**, 8328 (2009).
53. S.H. Lee, E. Cho, S.H. Jeon, and J.R. Youn, *Carbon*, **45**, 2810 (2007).
54. Q. Zhang, D.R. Lippits, and S. Rastogi, *Macromolecules*, **39**, 658 (2006).
55. Q. Zhang, S. Rastogi, D. Che, D. Lippits, and P.J. Lemstra, *Carbon*, **44**, 778 (2006).